Bio-Inspired Guidance Law — Interception While Avoiding an Obstacle

Research Project

Author: Hagar Berenstein
Advisor: Tal Shima

The Cooperative Autonomous Systems (CASY) Lab
Faculty of Aerospace Engineering, Technion

August 2025

Abstract

This research investigates a biologically inspired combined guidance law for interception with obstacle avoidance, based on the work of Fabian *et al.* who observed this law in the flight of a miniature robber fly. The law merges Proportional Navigation with an avoidance term proportional to the rate of change of the obstacle's angular size. Unlike prior work, we focus on scenarios where Proportional Navigation alone results in collision. The behavior of the guidance law was found to be highly sensitive to the chosen avoidance gain parameter c. For low values of c, the Proportional Navigation component dominates, and the interceptor often fails to avoid the obstacle. In contrast, for sufficiently high values of c, the avoidance becomes effective, resulting in a significant clearance distance from the obstacle. We also examined the influence of first-order dynamics and observed that they reduce the clearance distance and introduce a delay, sometimes causing the interceptor to maneuver around the obstacle from different sides. A field-of-view constraint was implemented but was found to have negligible impact on performance under the conditions tested. Finally, we compared the combined law with an optimal avoidance strategy derived for a point obstacle.

Contents

1 Literature Review 5
1.1 Interception Strategies in Nature 5
1.1.1 Geometric Rules 5
1.1.2 Guidance Laws 6
1.2 Obstacle Avoidance During Pursuit 6
1.2.1 Geometric Rules 7
1.2.2 Guidance Laws 7
1.2.3 Obstacle Avoidance in Nature 8
1.3 Conclusions from the Literature Review 8
2 Mathematical Model 9
2.1 Kinematic Equations (Interceptor and Target) 9
2.2 Filtered (Lag) Dynamics 10
2.3 Guidance law 11
2.4 Field of View (FOV) Condition 11
3 Simulation Results 11
3.1 Simulation of the combined guidance law 12
3.1.1 Scenario 1- Different initial position 12
3.1.2 Scenario 2- The effect of the gain c 16
3.1.3 Scenario 3- First order dynamics effects 19
3.2 Comparison with a different avoidance guidance law 23
3.2.1 Scenario 4 24
3.2.2 Scenario 5 25
3.2.3 Conclusions from the comparison 26
4 Conclusions 27
5 Possible Future Work 27
6 Appendix A- finding ϕ and its derivative 33

Nomenclature

a_M	Interceptor acceleration command in practice
a_{Mc}	Interceptor commanded acceleration
a_T	Target acceleration command in practice
a_{PN}	PN acceleration command
a_{MN}, a_{TN}	Acceleration components projected along normal directions (Kumar's law)
a_{MNo}	Obstacle avoidance acceleration command in Kumar's law for the case of a single obstacle
a_{obs}	Obstacle Avoidance acceleration command
c	Dimensionless parameter weighting the avoidance behavior
N	Navigation constant
r	The range between the target and the interceptor
r_{Mo}	The range between the interceptor and the obstacles's center
r_{MR}	The range between the interceptor and the obstacles's right bottom corner
r_{ML}	The range between the interceptor and the obstacles's left bottom corner
t_{go}	Time to interception
v_M	Interceptor velocity
v_T	Target velocity
V_c	The closing velocity
(x_M, y_M)	Interceptor's position in an inertial frame
(x_T, y_T)	Target's position in an inertial frame
δ	The angle between the LOS and v_M
γ	Path angle
$\dot{\gamma}$	Rate of change of the path angle
γ_D	Desired interception angle
γ_{M0}	Initial heading of missile
γ_{T0}	Initial heading of target
λ	Angle of LOS relative to a fixed point
$\dot{\lambda}$	Rate of change of the angle of LOS
λ_0	Initial value of LOS
ϕ	Angular size of obstacle — the angle between r_{ML} and r_{MR}
$\dot{\phi}$	Rate of change of angular size ϕ
θ	The angle between the LOS and v_T
τ	Time constant of first-order dynamics
ω	The angle between v_M and r_{Mo}

List of Abbreviations

PP Pure Pursuit
LOS Line of Sight
DPP Deviated Pure Pursuit
PN Proportional Navigation
PNP mixed guidance law PP+PN
UAV Unmanned Aerial Vehicle
APN Augmented Proportional Navigation
AV Autonomous Vehicle
FOV Field of View

1 Literature Review

The literature review will focus on research in the field of guidance, addressing all its components — from the geometric rule, through the guidance law, to the control mechanism. The geometric rule defines the kinematic behavior of the system, the guidance law specifies the algorithm that implements this rule, and the control mechanism ensures the stability of the inner control loop. In this review, the primary emphasis will be on the first two levels, and the focus will be mainly on bio-inspired guidance laws. In addition, we will review studies on obstacle avoidance during interception, both in general systems and in the animal domain.

1.1 Interception Strategies in Nature

Many animals use simple and effective strategies to intercept moving targets, making them a valuable source of inspiration for guidance systems. These natural behaviors often rely on basic geometric rules and can be modeled with guidance laws similar to those used in actual guidance systems. In this subsection, we focus on biologically inspired interception strategies to highlight the first two levels of the guidance process: the geometric rule and the guidance law.

1.1.1 Geometric Rules

Observing nature, we can gain valuable insights into existing geometric rules and potentially uncover different strategies. One rule is Line of Sight (LOS) geometric rule. According to this rule, the interceptor is always on the ray that starts at a reference point and passes through the target. [1]

Another rule is the Pure Pursuit (PP) geometric rule, which dictates that the pursuer velocity vector $\mathbf{v_M}$ coincides with the vector $\mathbf{r}$ (the range between the target and the pursuer in the LOS direction). Various examples of animal behaviors that exemplify the PP rule are presented in the literature. For instance, Shneydor [1] demonstrates that many parents have observed that most children of tender tend to chase one another according to the PP rule. A research on ants behavior is demonstrated in [2], in which a leading ant signals others to follow, maintaining a fixed distance while aligning their movement towards the one ahead, and actually implementing this geometric rule too. In a related study, Kane [3] explains that goshawks use the PP rule when capturing stationary prey. Furthermore, houseflies have been shown to employ this strategy when chasing mates [4], and similar behavior has been observed in teleost fish when tracking moving food [5].

Next, we consider the Deviated Pure Pursuit (DPP) rule, where $\mathbf{v_M}$ leads $\mathbf{r}$, where 'leads' means 'In the direction of the future position of T'. Shneydor [1] further noted that this strategy is intuitively employed by children around the age of three or four, as well as by certain species of cats and night insects that approach light sources. McHenry *et al.* [6] reveal that bluefish utilize the DPP rule when pursuing prey fish.

Another relevant geometric rule is Parallel Navigation, in which the direction of the LOS is maintained parallel to the initial LOS. Mathematically, this implies that the rate of rotation of the LOS vector is zero. This rule is employed by bats when chasing prey, as shown by Ghose *et al.* [7]. Similarly, Kane [3] reports that goshawks use Parallel Navigation when capturing moving prey, same as falcons when pursuing maneuvering targets [8].

We have discussed the geometric rule as implemented by children, but what about adults? A research by Fajen *et al.* [9] about people going by foot towards a moving target showed that their interception behavior exhibits dynamics that include an initial turn onto a straight path with a heading that leads the target, and a final decrease in the angle at the end of the approach. This strategy might be described as the known parallel navigation.

Another rule observed both in baseball players chasing fly balls [10] and in dogs pursuing frisbees [11] is the Liner Optical Trajectory. This strategy results when the pursuer's running

speed and direction maintain a rate of change in the horizontal optical angle, that matches the rate of change in the vertical optical angle.

Some geometric behaviors cannot be explained by current geometric rules. For example, G. Ribak *et al.* show in [12] that damselflies can adjust their trajectory to minimize the angle between their longitudinal axis and the line of sight to the target—without altering body yaw.

1.1.2 Guidance Laws

Now, we shift our focus to the second level—the guidance law. Initially, we will examine Proportional Navigation (PN), a guidance law that implements parallel navigation, which is widely employed in guided interceptor systems. As explained in [13], PN issues acceleration commands, perpendicular to the instantaneous interceptor-target LOS, which are proportional (by a proportionality constant known as the Navigation constant (N)) to the LOS rate and closing velocity. As demonstrated in [14], the terminal attack trajectories of peregrine falcons align with this guidance law. A notable case is presented in [15], where it is explained that the trajectories of both captive-bred gyrfalcons and peregrine falcons is modeled by PN. In addition, the analysis in [16] reveals that pigeons steering toward vertical gaps follow flight trajectories well-modeled by PN with estimated navigation constant (N) of about 2.6, which closely matches the theoretical optimum of 3. Additionally, Fabian *et al.* [17] show that two species of robber flies employ PN: *Holcocephala* with N = 3, and *Coenosia* with N = 1.5, the latter exhibiting a shorter time delay. This suggests that *Coenosia* can adjust its flight path with minimal lag, reducing the risk of missing a rapidly maneuvering target. In contrast, the longer time delay in *Holcocephala* implies a more predictive approach, relying on internal models to compensate for the delay. Moreover, in [18] it is shown that the tiger beetle adopts this guidance law as well, with a delay of one half-stride.

Certain animals do not adhere to conventional guidance laws. For example, in [15],[19] it is presented that the attack trajectories of Harris' hawks are best modeled by a mixed guidance law PP+PN (PNP) coupling low-gain proportional navigation with a low-gain pure pursuit. In [20], it is distinguished between inertial-PNP, which uses inertial measurements of the line-of-sight rate, and background-PNP, which estimates the line-of-sight rate relative to the visual background. It is shown there that inertial-PNP provides the closest fit to the data of the hawks' pursuit trajectories. Another animal that exhibits a mixed guidance strategy combining PP and PN is the blowfly, as described in [21].

Another strategy is shown in [22], where it is shown that the dragonfly's interception strategy is based on prey fixation, where predictive head rotations stabilize the prey's image.

In [23] it is suggested that dragonflies *(Hemianax papuensis)* actively use Motion Camouflage to disguise themselves as stationary during territorial aerial maneuvers. This method is further explained by Justh *et al.* in [24], where a biologically plausible guidance law is proposed for this method. It is explained that it uses range information to support a high gain in the initial phase of the engagement, ramping down to a lower value in the terminal phase.

One more strategy is presented in [25], involving the *Holcocephala fusca* robber flies, previously discussed in the context of PN. While the initial phase of pursuit follows the PN guidance law, the study reveals that in the final stage—approximately 29 cm from the target—the flies switch to an interception strategy which is described as a "lock-on" process. This phase is characterized by a new heading and a speed slightly exceeding that of the prey.

1.2 Obstacle Avoidance During Pursuit

During the interceptor's trajectory toward the target, it is common for obstacles—such as aircraft crossing the interceptor's path—to interfere. This challenge has been the subject of extensive research, and we will highlight some notable findings in this area.

There is a wide research about the way autonomous vehicles (AVs) are guided to avoid obstacles, some of them are presented here. In [26] it is explained about "The Electric Field Model" as a way to avoid obstacles. This approach consists of two main components: an egocentric risk map representing obstacles, and a potential field model that treats obstacles as repelling charges, guiding the vehicle like an electron through the field. Another approach is shown in [27], where the main idea is to present a path planning method for autonomous vehicles that uses a parametric sigmoid function and a rolling horizon strategy to generate smooth paths in real time. Lowe *et al.* [28] show Emergency Obstacle Avoidance Maneuver methodology for AVs traveling at higher speeds and lower road surface friction using optimization. The optimization minimizes the total longitudinal distance traveled during an emergency maneuver by adjusting acceleration and steering inputs, subject to vehicle dynamics and control constraints.

1.2.1 Geometric Rules

Obstacle avoidance during pursuit has been studied through several geometric and control strategies. A collision cone method for detecting and avoiding collisions between moving objects with constant relative velocities was proposed in [29], while [30] introduced velocity obstacles to select safe velocities without requiring full trajectory integration. The environment partitioning technique of avoidance maps was developed in [31] and further optimized in [32] to improve computational efficiency and reduce control effort. In [33], Giovannangeli *et al.* propose geometric constraints to deal with a two-players pursuer evader games in presence of a single unknown convex obstacle.

Geometric path planning approaches have also been explored. In [34], Bernstein–Bézier curves, previously applied for single-robot guidance in [35], are extended to multi-robot collision avoidance, generating smooth paths that respect velocity and acceleration constraints. An alternative, analytically feasible method using Four Parameter Logistic curves was proposed in [36], offering closed-form S- and half-S-shaped continuous-curvature paths with fewer design parameters compared to Bézier, B-spline [37], and clothoid[1] -based approaches. As shown in [38], General scale of $O(\sqrt{h} + \log(n))$ pursuers can deterministically capture an evader in any polygon with n vertices with h obstacles under equal speed assumptions.

1.2.2 Guidance Laws

Several guidance laws has been found for avoiding obstacles while pursuing, and some will be presented here. In [39], for instance, a collision avoidance algorithm for Unmanned Aerial Vehicles (UAV) based on PN guidance is proposed, modeling both the UAV and obstacle as particles in a 2D plane and guiding the UAV's relative velocity toward a safety boundary while ensuring stability. In [40], Anderson *et al.* present an optimal-stopping control method for collision avoidance and return-to-course flight without requiring prior knowledge of collision timing, showing improved maneuvering efficiency and minimal path deviation compared to predefined stopping strategies.

Several works have extended classical Augmented Proportional Navigation (APN) guidance to include obstacle avoidance. For example, in [41], Weiss *et al.* showed that linear quadratic optimal control, and techniques developed in [42], can produce guidance laws with this form for intercepting maneuvering targets while avoiding a single obstacle. Kumar *et al.* [43] generalized this approach to handle multiple obstacles and imposed an intercept angle constraint. Building on these ideas, Jha *et al.* [44] proposed a cooperative guidance law for $n - on - n$ engagements, extending APN by incorporating collision avoidance among pursuers while minimizing team effort, with closed-form results for the 2-on-2 case validated through simulations and experiments.

[1] A clothoid is a type of curve whose rate of change of curvature varies linearly with distance.(MathWorks)

In addition, [45] proposes a hybrid feedback law for spherical obstacle avoidance in $\mathbb{R}^n$, guaranteeing global asymptotic stabilization with robust switching between motion-to-goal and obstacle-avoidance modes.

1.2.3 Obstacle Avoidance in Nature

Some research has been conducted about the way animals pursuit while avoiding obstacles in their way. Fabian *et al.* [46] describe this kind of flight of the fly *Holcocephala fusca* as the result of two competing navigational systems: PN and a simple obstacle avoidance algorithm. This model, termed *combined guidance*, integrates obstacle avoidance and target interception by activating the second component only when obstacles appear to increase in angular size ($\dot{\phi} > 0$), indicating potential collision. It assumes the pursuer visually fixates on the target, leading to a limited field of view, and only considers obstacles within a certain angular range of the LOS to the target. It is fascinating that similarities can be found here to the form of the guidance law for multiple-obstacle avoidance obtained by Kumar *et al.* in [43]. How exactly the two guidance systems, potentially operating at different time delays (∼30 ms for PN and ∼90 ms for obstacle avoidance), are integrated to form a response is uncertain but worthy of interest.

Another example is reported in [47], Harris' hawks continue to follow a mixed guidance law (PNP) during obstructed pursuit. However, they appear to apply an additional discrete steering adjustment, redirecting their flight path to maintain a clearance of approximately one wing length from an upcoming obstacle, once they reach a specific distance threshold. In addition, as shown in [48], big brown bats avoid obstacles during pursuit by actively steering their sonar beam and aligning head direction with flight control. A different example is shown in [49], where it is suggested the locusts initiate avoidance when the obstacle in the flight path exceeds a retinal image size of around 10 degrees. Fajen *et al.* show in [50] that humans can navigate and pursue targets while avoiding obstacles using real-time information-based control, without relying on an internal map or complex path planning. Instead, movement emerges from continuous local adjustments to goals and surrounding obstacles.

1.3 Conclusions from the Literature Review

This literature review reveals that many animal species employ guidance strategies that can be modeled using classical geometric rules such as PP, DPP, and Parallel Navigation. While some species rely on simple, consistent rules, some use mixed guidance laws or rely on other strategies (such as the Motion Camouflage shown in [24]).

In addition, a wide range of geometric and control-based strategies for obstacle avoidance during pursuit has been investigated, from deterministic capture methods and techniques to optimal path planning. Extensions of classical guidance laws, particularly PN, have been developed to incorporate obstacle avoidance, both through optimal control frameworks and hybrid switching strategies. Additionally, various species exhibit the ability to pursue targets while avoiding obstacles, integrating real-time steering adjustments, such as the combined law for obstacle avoidance observed in flies in [46]. Despite these insights, there remains much to discover about understanding and then formalizing and translating natural obstacle avoidance mechanisms into practical applications.

2 Mathematical Model

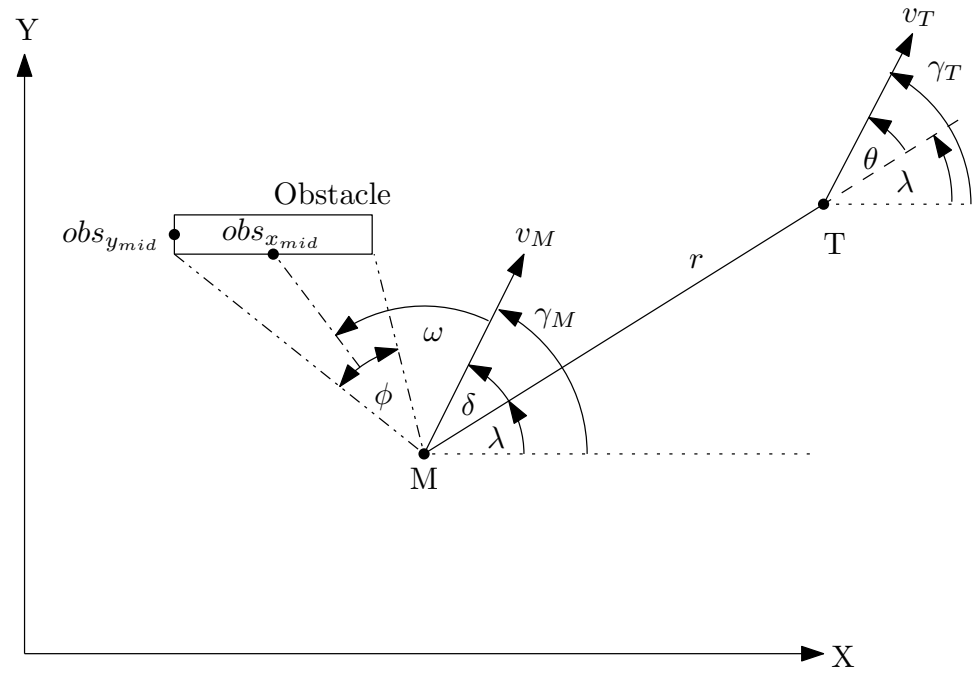

Figure 1: Geometric description

This research investigates the guidance law employed by flies during obstacle avoidance, as inspired by the findings in [46]. The engagement is analyzed in a two-dimensional plane, with the obstacle modeled as a bar-shaped object. Both the interceptor and the target are represented as point masses.

2.1 Kinematic Equations (Interceptor and Target)

The geometric description is shown in Figure (1). The positions of the interceptor and target evolve based on their respective headings and speeds:

$$\dot{x}_M = v_M \cos(\gamma_M) \tag{1}$$

$$\dot{y}_M = v_M \sin(\gamma_M) \tag{2}$$

$$\dot{x}_T = v_T \cos(\gamma_T) \tag{3}$$

$$\dot{y}_T = v_T \sin(\gamma_T) \tag{4}$$

where x is the position, v is the velocity and γ is the heading angle.

The interceptor acceleration command $a_{Mc}(t)$ is given by

$$a_{Mc}(t) = a_{\text{PN}}(t) + a_{\text{obs}}(t)\, \mathbf{1}_{\{\dot{\phi}(s)>0\ \forall s\leq t\}}, \tag{5}$$

where a_{PN} is the acceleration resulting from the pure pursuit (PN) guidance law, and a_{obs} is the acceleration component responsible for obstacle avoidance. The indicator function $\mathbf{1}_{\{\dot{\phi}(s)>0\ \forall s\leq t\}}$ equals 1 as long as the rate of change of the obstacle's angular size, $\dot{\phi}$, has never been negative up to time t, and 0 afterwards.

In other words, the avoidance acceleration a_{obs} is applied only while $\dot{\phi} > 0$, which indicates that the interceptor is approaching the obstacle. Once $\dot{\phi}$ becomes negative—meaning the interceptor is moving away from the obstacle—a_{obs} is set to zero, regardless of any subsequent

increase in $\dot{\phi}$. This prevents singularities as the interceptor passes the obstacle and is consistent with scenarios involving a single obstacle. Meanwhile, a_{PN} remains active throughout, ensuring that the interceptor continues to pursue the target.

The law was derived and tested in the context of flies avoiding a single obstacle, and therefore it cannot be assumed to represent the general avoidance behavior of flies in more complex environments. In reality, flies are not limited to encountering only one obstacle, and their navigation strategies are likely to involve more sophisticated mechanisms when multiple obstacles are present.

2.2 Filtered (Lag) Dynamics

When implementing first-order dynamics, the acceleration does not instantaneously reach its desired value, but rather converges to it exponentially. This behavior is characterized by the system's time constant, typically denoted as τ. A smaller time constant results in a faster response, meaning the acceleration approaches its desired value more quickly. Conversely, a larger time constant leads to slower convergence. This exponential convergence models physical systems more realistically, particularly in the presence of actuator dynamics or response delays. Single-lag dynamics is defined:

$$G(s) = \frac{1}{1+\tau s} \tag{6}$$

And in time domain:

$$a_M(t) + \tau \frac{da_M}{dt} = a_{Mc} \tag{7}$$

The heading rate of the interceptor is related to its lateral acceleration:

$$\dot{\gamma}_M = \frac{a_M}{v_M} \tag{8}$$

When no dynamics is implemented, the acceleration command a_{Mc} is equal to the acceleration in practice a_M.

$$\dot{\gamma}_T = \frac{a_T}{v_T} \tag{9}$$

We will assume constant velocity for the target, i.e. $a_T = 0$ and therefore:

$$\dot{\gamma}_T = 0 \tag{10}$$

Relative Geometry and LOS Rate

Let the distance between interceptor and target be:

$$r = \sqrt{(x_T - x_M)^2 + (y_T - y_M)^2} \tag{11}$$

the LOS angle λ and its rate of change is defined:

$$\lambda = \arctan\left(\frac{y_T - y_M}{x_T - x_M}\right) \tag{12}$$

$$\dot{\lambda} = \frac{(x_T - x_M)(\dot{y}_T - \dot{y}_M) - (y_T - y_M)(\dot{x}_T - \dot{x}_M)}{r^2} \tag{13}$$

2.3 Guidance law

The guidance law for interception while avoiding an obstacle, as presented in [46], is as follows:

$$\dot{\gamma} = N\dot{\lambda} + \text{sign}(\omega)c\dot{\phi}$$

While using (8) we get:

$$a_{Mc} = v_M \cdot N \cdot \dot{\lambda} + v_M \cdot \text{sign}(\omega)c\dot{\phi} \tag{14}$$

The terms of equation (14) are as follows. The first part is the well-known PN. The variable ω represents the bearing of the obstacle relative to the pursuer's heading, while sign(ω) indicates the direction of the obstacle relative to the pursuer—specifically, whether it lies to the left or right. The constant c is a dimensionless parameter that weights the avoidance behavior, influencing how strongly the interceptor reacts to nearby obstacles. The symbol ϕ denotes the angular width of the obstacle, and $\dot{\phi}$ refers to the rate of change of this angular size, which becomes positive when the obstacle appears to grow in the pursuer's field of view. It characterizes the rate at which the interceptor is approaching or moving away from the obstacle. The way to find ϕ and $\dot{\phi}$ is shown in Appendix A.

Proportional Navigation:

$$a_{\text{PN}} = N \cdot v_M \cdot \dot{\lambda} \tag{15}$$

Obstacle Avoidance:

$$a_{\text{obs}} = c \cdot v_M \cdot \text{sign}(w) \cdot \dot{\phi} \tag{16}$$

2.4 Field of View (FOV) Condition

The guidance logic is activated only if the target is within the interceptor's field of view. Let

$$\delta = \gamma_M - \lambda \tag{17}$$

where δ is the angle between r and v_M. Then the guidance laws are applied only if:

$$|\delta| \leq 0.5 \cdot \text{FOV} \tag{18}$$

outside the FOV, $a_{PN} = 0$. Similarly:

$$|\omega| \leq 0.5 \cdot \text{FOV} \tag{19}$$

where ω is the angle between the interceptor's velocity and r_{Mo}, the position vector from the origin to the horizontal midpoint of the obstacle.

The obstacle avoidance acceleration a_{obs} is applied only when the obstacle lies within the interceptor's field of view. If the obstacle is outside the field of view, a_{obs} is set to zero.

3 Simulation Results

The initial conditions are listed in Table 1, and the simulation scale is based on [17, 46]. Since the guidance law is biologically inspired by insect flight, particularly that of flies, the parameters are intentionally small.

Table 1: Simulation parameters

Parameter	**Value**
Target speed v_T	$320\,\mathrm{mm\,s^{-1}}$
Velocities ratio $K = \frac{v_M}{v_T}$	1.5
Target acceleration a_T	$0\,\mathrm{mm\,s^{-2}}$
Initial target heading γ_T	0 rad
PN constant N	3.6
Obstacle width (x) obs_{width}	25 mm
Obstacle height (y) obs_{height}	1 mm

The interceptor's initial position varies across the different scenarios, while the obstacle size remains constant. No acceleration limits are applied. It was observed that imposing a FOV constraint had no noticeable impact on the results. Therefore, the simulations presented here are conducted without an FOV limitation; however, the outcomes are comparable to those obtained with a 130° FOV.

3.1 Simulation of the combined guidance law

The simulation was conducted using MATLAB, employing the Euler integration method with a fixed time step of $1 \cdot 10^{-3}[s]$. During the simulation, we examined different cases of obstacle evasion including cases in which only PN was performed, resulting in a collision with the obstacle. This was done for comparison purposes and to highlight the differences. Even in cases where a collision with the obstacle occurred, we deliberately continued the simulation until interception.

3.1.1 Scenario 1- Different initial position

First, we will show the simulation results for different initial positions, with small values of c, similar to those that are found to be used by flies in [46]. Figure (2) shows the interceptor's trajectory for different values of c, where the black horizontal bar denotes the obstacle. The parameters of this scenario are shown in Table 2.

Table 2: Scenario 1 (a)- avoiding from the right side- configuration summary

Parameter	**Value**
Interceptor initial position (x_{M0}, y_{M0})	$(340\,\mathrm{mm}, -300\,\mathrm{mm})$
Initial interceptor heading γ_M	90°
Initial target position (x_{T0}, y_{T0})	$(0.1\,\mathrm{mm}, 0.1\,\mathrm{mm})$
Obstacle center $(obs_{x_{\mathrm{mid}}}, obs_{y_{\mathrm{mid}}})$	$(270, -70)$ mm
Interceptor dynamics	None

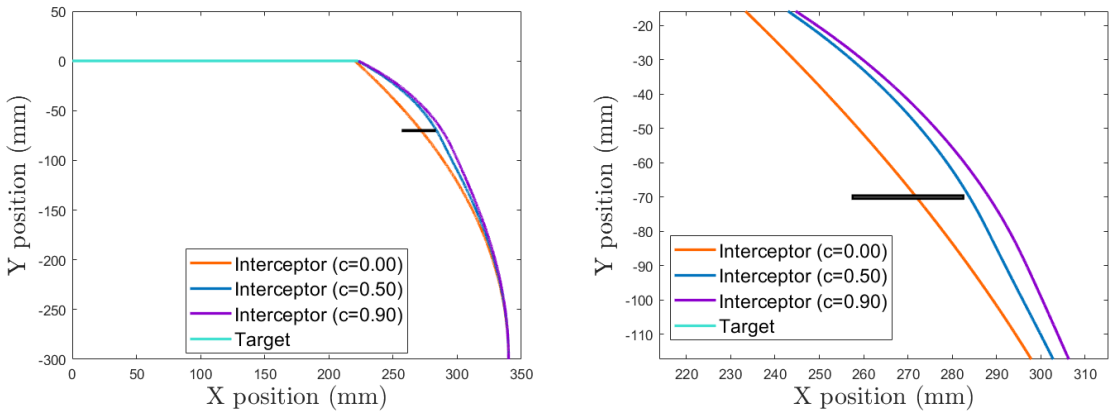

Figure 2: Interceptor trajectories with combined (flies) guidance law for scenario-1 (left: full view, right: zoomed).

From Figure (2) we can see that when $c = 0$, the guidance law reduces to PN, in which the interceptor does not avoid the obstacle. It can be seen that for larger values of c the avoidance is more significant, as expected. The zoomed-in graph highlights that for each gain that was chosen- the interceptor is avoiding the obstacle successfully.

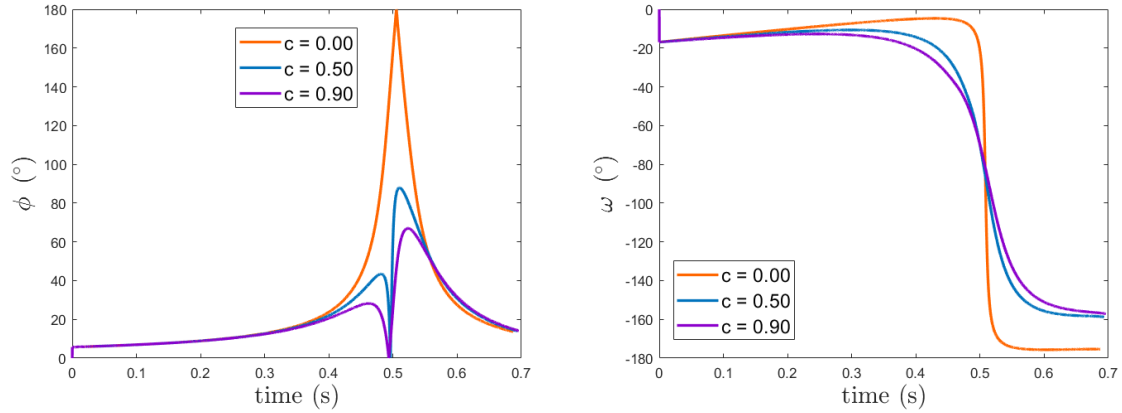

Figure 3: Left: Angular obstacle size ϕ over time. Right: The angle ω between v_M and r_{Mo} as function of time

The plot of $\phi(t)$ on the left of Figure (3) illustrates the angular size of the obstacle as a function of time. For the case of $c = 0$, as expected, the angle reaches its maximum value of 180° when the interceptor collides with the obstacle. As the interceptor approaches the obstacle, the angle increases, and as it moves away, the angle decreases accordingly. For $c > 0$, the angle initially increases as the interceptor approaches the obstacle. However, when the interceptor reaches the same y-coordinate as the obstacle, the angle decreases toward zero. It then increases again briefly before finally decreasing as the interceptor moves further away. The sign of ω indicates whether the interceptor is positioned to the left or right of the obstacle. Throughout the flight, ω remains negative, which implies that the interceptor approaches from the right side.

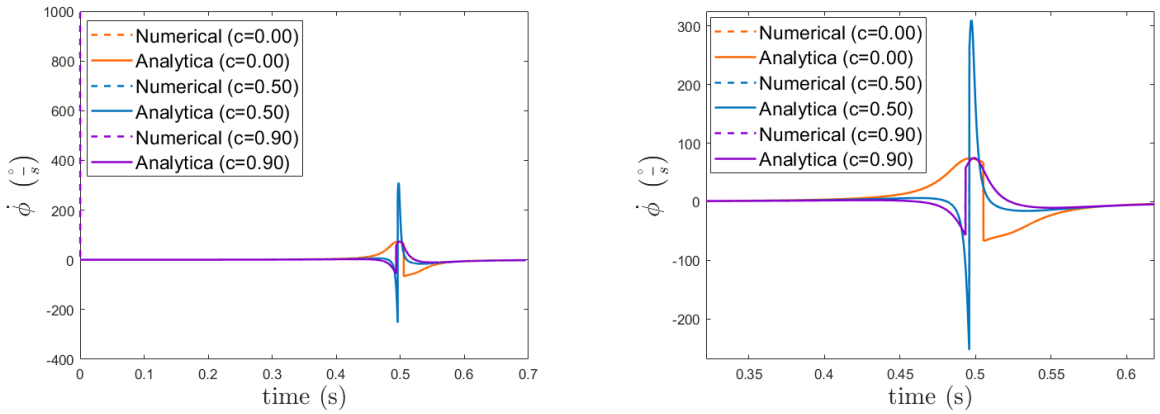

Figure 4: Rate of change of the obstacle's angular size $\dot{\phi}$ (left: full view, right: zoomed).

As expected, when the angle ϕ increases, its derivative $\dot{\phi}$, presented in Figure (4) is positive. Initially, $\dot{\phi} > 0$, while toward the end of the trajectory, $\dot{\phi} < 0$. Additionally, abrupt changes in the derivative can be observed when the interceptor reaches the same height as the obstacle. It can also be seen that the analytical and numerical calculations of the derivative closely coincide, which confirms the accuracy of the computation.

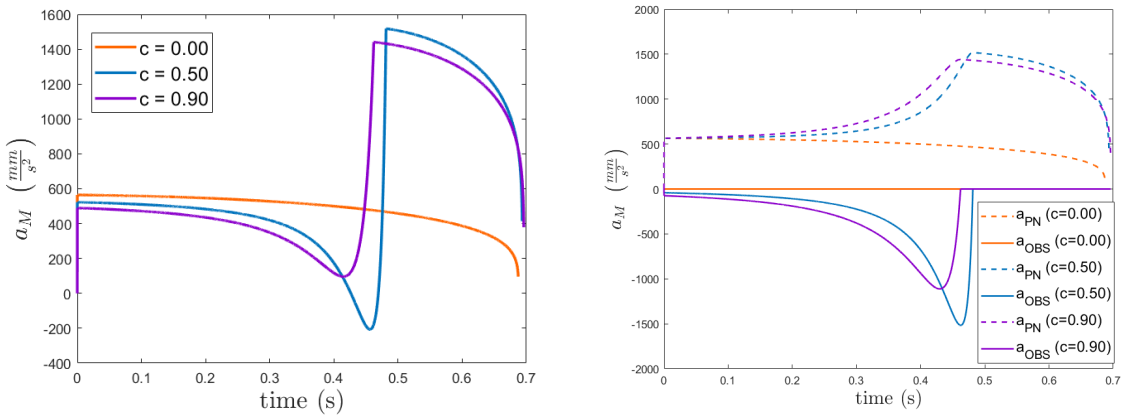

Figure 5: Left: Interceptor acceleration a_M over time. Right: Comparison between a_{PN} and a_{OBS} components.

The right graph in Figure (5) illustrates how each acceleration component contributes to the total commanded acceleration. For $c = 0$, as expected, $a_{obs} = 0$. For positive values of c, we observe that when $\dot{\phi}$ is negative, a_{obs} remains zero. However, when $\dot{\phi}$ is positive, the obstacle avoidance component becomes negative and increases in magnitude as $\dot{\phi}$ grows.

We will now change the interceptor's initial position to see the avoidance from the other side. The parameters are shown in Table 3.

Table 3: Scenario 1 (b)- avoiding from the left side- configuration summary

Parameter	**Value**
Interceptor initial position (x_{M0}, y_{M0})	$(450\,\text{mm}, -300\,\text{mm})$
Initial interceptor heading γ_M	150 °
Initial target position (x_{T0}, y_{T0})	$(0.1\,\text{mm}, 0.1\,\text{mm})$
Obstacle center $(obs_{x_{\text{mid}}}, obs_{y_{\text{mid}}})$	$(270, -70)$ mm
Interceptor dynamics	None

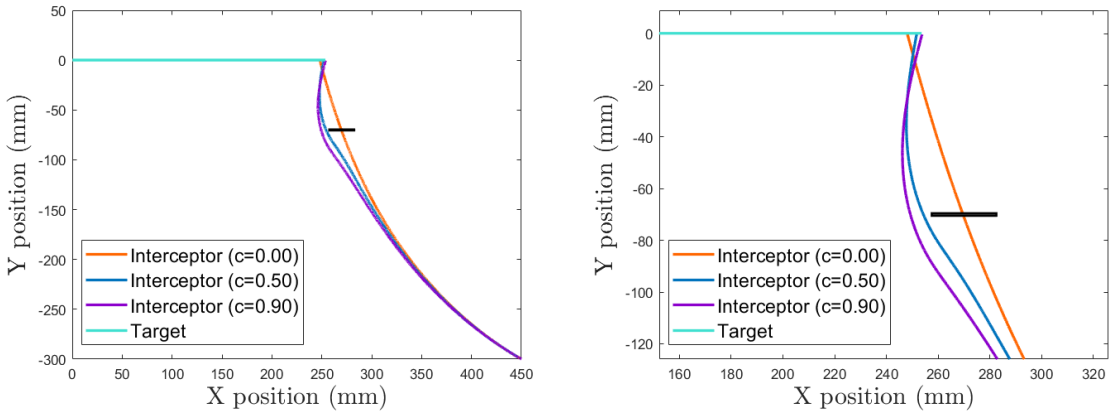

Figure 6: Interceptor trajectories with combined (flies) guidance law (left: full view, right: zoomed).

Figure (6) shows that for all values of c, the interceptor successfully avoids the obstacle, with the evasion occurring this time from the left side. Moreover, the larger the value of c, the more pronounced and significant the evasion becomes. In all cases, the interception itself is successfully achieved.

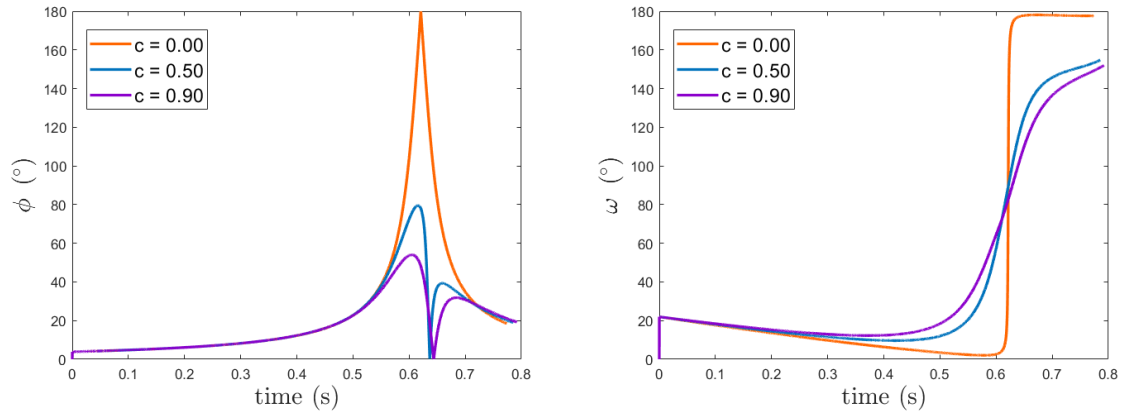

Figure 7: Left: Angular obstacle size ϕ over time. Right: The angle ω between v_M and r_{Mo} as function of time

It can be seen in the graph on the right in Figure (7) that this time ω is positive, so the

interceptor is avoiding the target from the left. In the left part we can see the obstacle angular size as function of time which gives similar results as in the previous case.

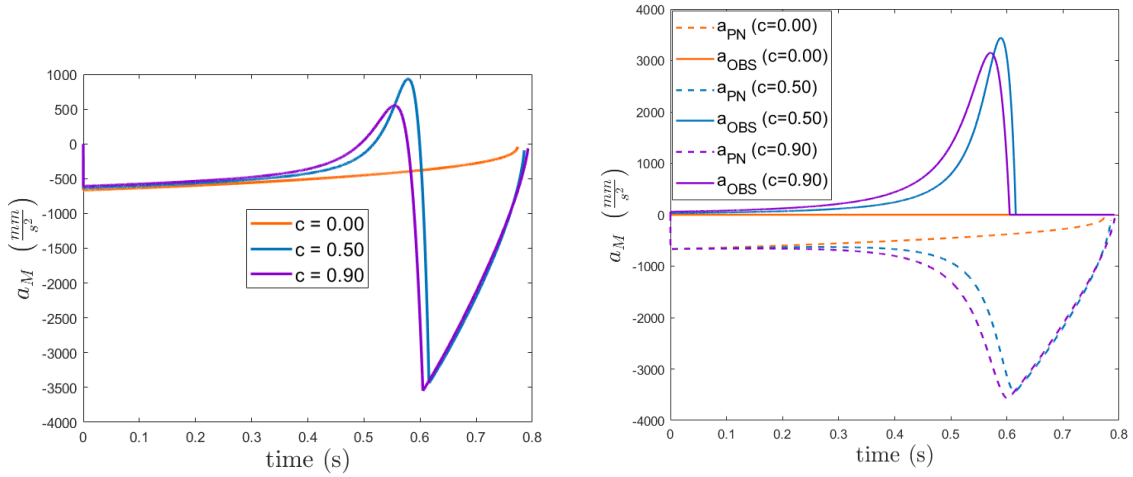

Figure 8: Left: Interceptor acceleration a_M over time. Right: Comparison between a_{PN} and a_{OBS} components.

We note that this time, the acceleration component of the obstacle evasion, as shown in Figure (8), is positive in accordance with the sign of ω, while the PN acceleration component is negative, so the acceleration components still act in opposition to each other.

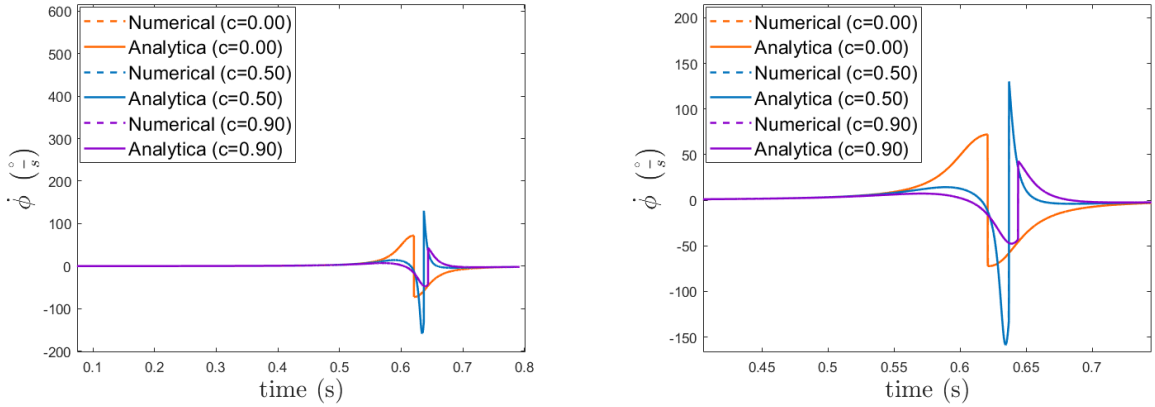

Figure 9: Rate of change of the obstacle's angular size $\dot{\phi}$ (left: full view, right: zoomed).

In Figure (9), the derivative of ϕ as a function of time is shown. As expected, when the angle increases, the derivative is positive, and vice versa. In addition, from the moment the derivative becomes negative, the evasion acceleration drops to zero.

3.1.2 Scenario 2- The effect of the gain c

In this section, we compare the trajectories resulting from small ($c = 0.2$) and large ($c = 5$) values of c to observe how the gain influences the interceptor's path.

Table 4: Scenario 2- configuration summary

Parameter	**Value**
Interceptor initial position (x_{M0}, y_{M0})	$(450\,\text{mm}, -300\,\text{mm})$
Initial interceptor heading γ_M	150 °
Initial target position (x_{T0}, y_{T0})	$(0.1\,\text{mm}, 0.1\,\text{mm})$
Obstacle center $(obs_{x_{\text{mid}}}, obs_{y_{\text{mid}}})$	$(270, -70)$ mm
Interceptor dynamics	None

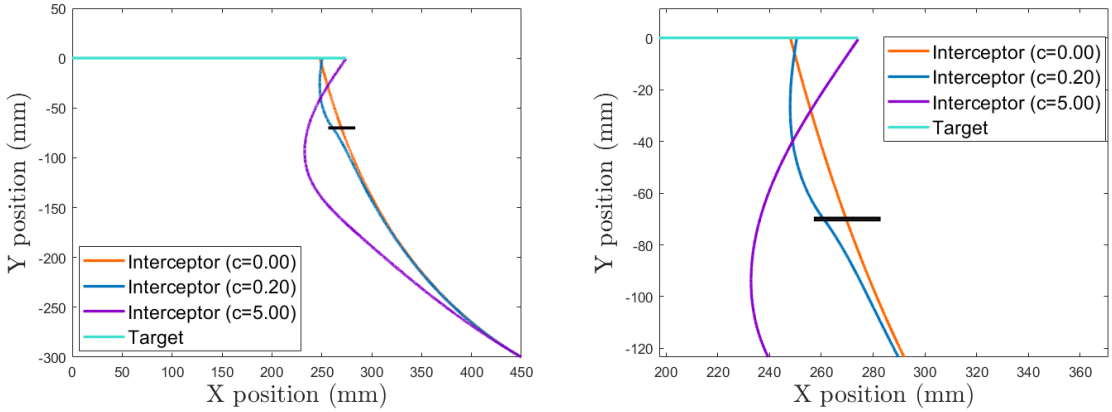

Figure 10: Interceptor trajectories with combined (flies) guidance law (left: full view, right: zoomed).

As shown in Figure (10), when the avoidance gain is too small ($c = 0.2$), it is insufficient to steer the interceptor away from the obstacle, resulting in a collision. In contrast, with a significantly larger gain of $c = 5$, the interceptor not only avoids the obstacle successfully but does so with a considerable clearance distance.

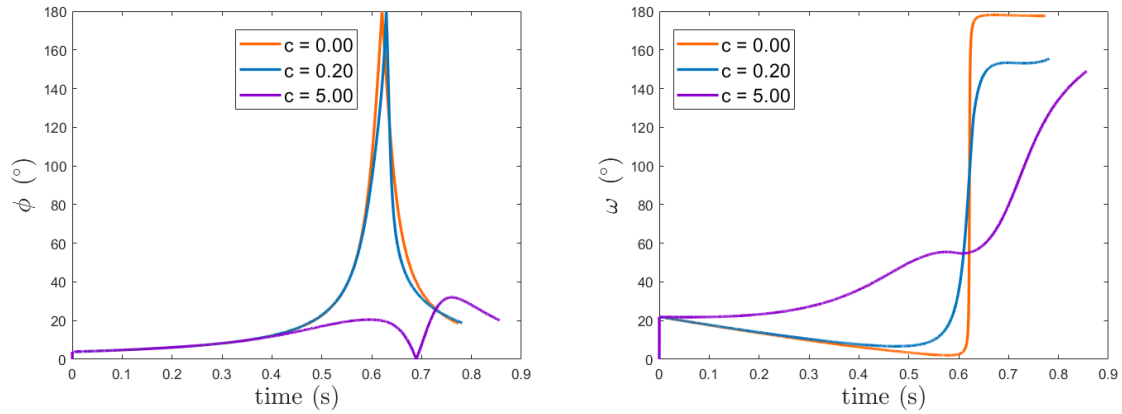

Figure 11: Left: Angular obstacle size ϕ over time. Right: The angle ω between v_M and r_{Mo} as function of time

On the left of Figure (11) it is seen that for $c = 0.2$, which is too small to avoid, the angular size of the obstacle resembles the one of $c = 0$. It is clear because when the interceptor

goes through the obstacle the angular distance is maximal. For a large gain, such as $c = 5$, the angular size changes only slightly. This behavior is expected, as the avoidance component dominates the guidance response. On the right side of the graph, it can be seen that for these initial conditions the interceptor will try to avoid from the left ($\omega > 0$) for each gain.

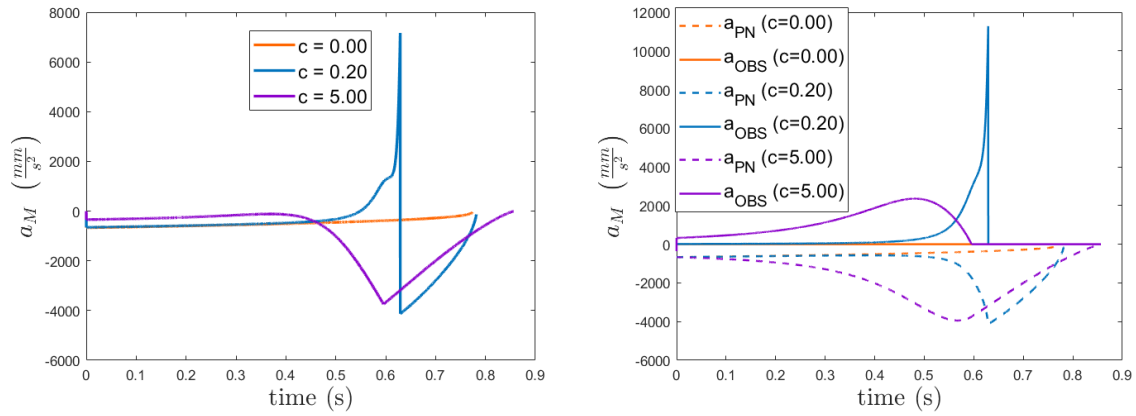

Figure 12: Left: Interceptor acceleration a_M over time. Right: Comparison between a_{PN} and a_{OBS} components.

In Figure (12), the right-hand side shows that for a high avoidance gain c, the interceptor exhibits a significant avoidance acceleration component a_{obs} from the very beginning of the flight. In contrast, for low values of c, the a_{obs} component remains nearly zero until the interceptor approaches the obstacle. As illustrated, when the gain is too small, even a sharp increase in avoidance acceleration near the obstacle is insufficient to prevent a collision, as it occurs over too short a time interval.

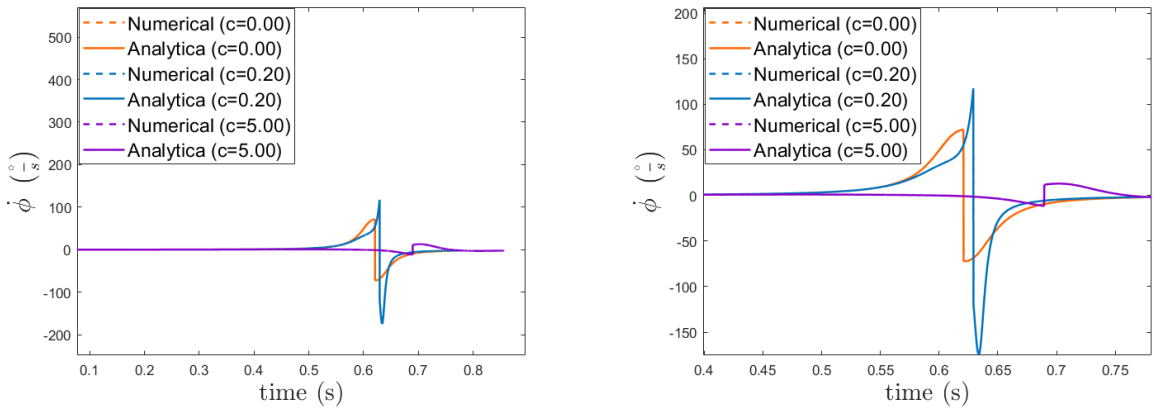

Figure 13: Rate of change of the obstacle's angular size $\dot{\phi}$ (left: full view, right: zoomed).

In Figure (13), it is evident that for larger values of c, the variation in $\dot{\phi}$ is smaller, and the value remains positive for a longer duration. Since the avoidance component is only active until $\dot{\phi}$ becomes negative, we observe that for $c = 0.2$, it is activated only briefly.

3.1.3 Scenario 3- First order dynamics effects

Up to this point, no dynamics have been applied to the interceptor. Next, we examine the effect of first-order dynamics on the interceptor's behavior. The time constant of the dynamics is significantly small due to the scale of the system, as it involves small flying objects with a very short time-to-go.

Table 5: Scenario 3 (a) configuration summary

Parameter	**Value**
Interceptor initial position (x_{M0}, y_{M0})	$(340\,\text{mm}, -300\,\text{mm})$
Initial interceptor heading γ_M	$90°$
Interceptor dynamics	First-Order
Dynamics time constant τ	$3 \cdot 10^{-5}\,\text{s}$

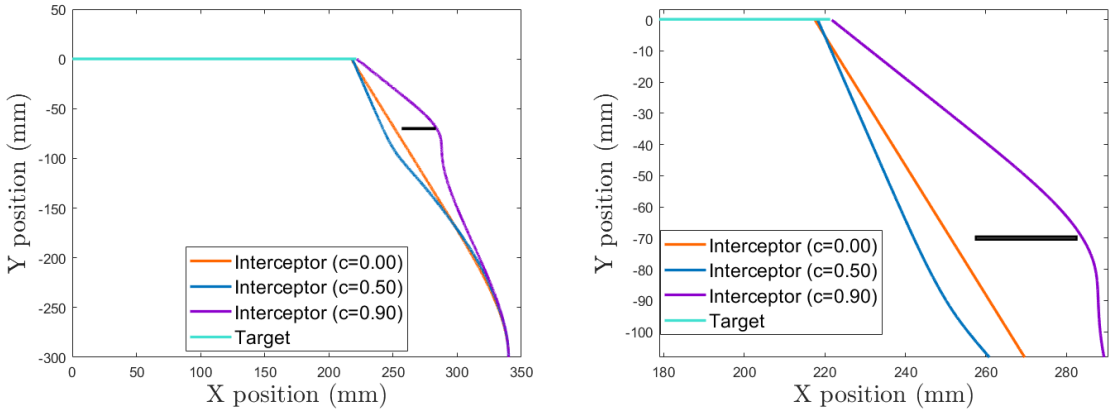

Figure 14: Interceptor trajectories with combined (flies) guidance law with dynamics (left: full view, right: zoomed).

We will compare the trajectories with first-order dynamics in Figure (14) to the trajectories with the same initial conditions without dynamics in Figure (2). First, for $c = 0$, we observe that under PN guidance, the interceptor does not collide with the obstacle. This outcome is due to the delay introduced by the interceptor's dynamics and should not be considered a general result. It is interesting that with dynamics, the interceptor is avoiding the obstacle from different directions for $c = 0.5, c = 0.9$, while without dynamics — it has avoided the obstacle from the right for any value of c. It might be caused from the delay that the dynamics cause, the interceptor takes longer to respond, and the avoidance is delayed.

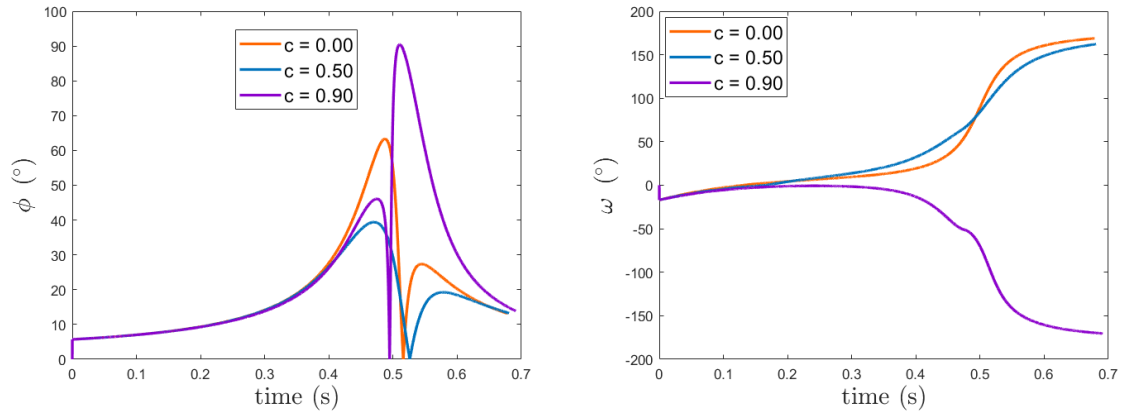

Figure 15: Left: Angular obstacle size ϕ over time. Right: The angle ω between v_M and r_{Mo} as function of time

On the right of Figure (15), we observe that for $c = 0.9$, the angle ω is negative, indicating that the interceptor avoids the obstacle from the right—unlike lower gain values, where avoidance occurs from the left. On the left side of the graph, the angular size initially increases as the interceptor approaches the obstacle, then drops sharply once it passes by, briefly increases again, and finally decreases as it continues toward the target.

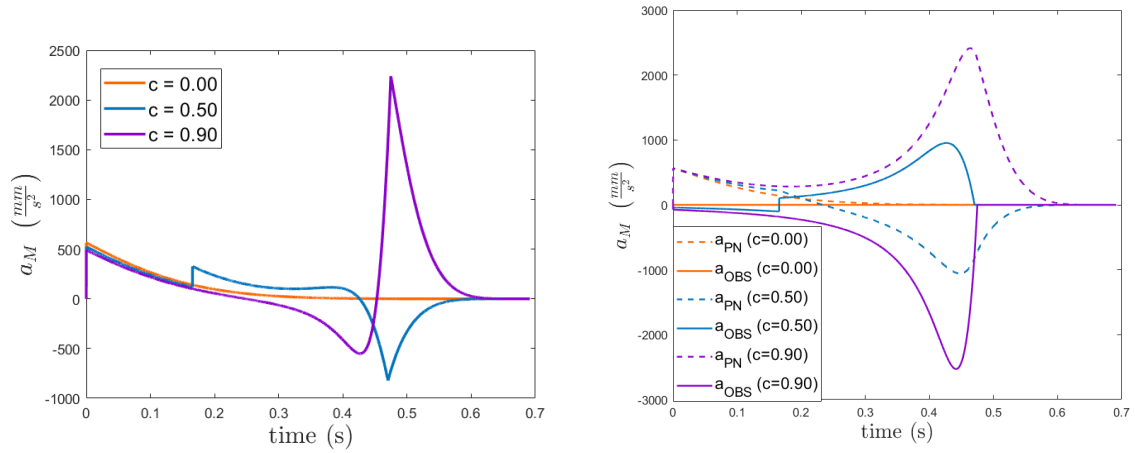

Figure 16: Left: Interceptor acceleration a_M over time. Right: Comparison between a_{PN} and a_{OBS} components.

On the right side of Figure (16), we observe that the sign of the avoidance component matches the sign of ω, as expected. Additionally, for higher gain values, the avoidance acceleration is stronger, which in turn results in a larger PN component—since it must compensate for the significant deviation from the trajectory toward the target. Consequently, on the left side of the graph, we observe that higher gain values result in larger acceleration peaks.

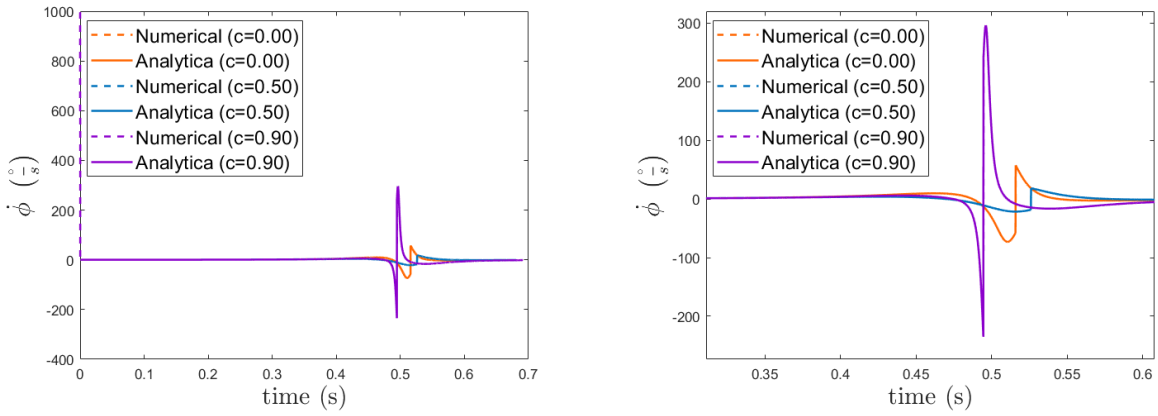

Figure 17: Rate of change of the obstacle's angular size $\dot{\phi}$ (left: full view, right: zoomed).

In Figure (17), $\dot{\phi}$ is shown as a function of time. As expected, for the case where the evasion distance is the smallest ($c = 0.9$), the changes in the derivative are the most abrupt. This is because the angular distance to the obstacle changes most sharply when approaching it, reaching a maximum and then decreasing significantly when moving away.

Now we will change the initial position of the interceptor.

Table 6: Scenario 3 (b)- configuration summary

Parameter	**Value**
Interceptor initial position (x_{M0}, y_{M0})	$(450\,\text{mm}, -300\,\text{mm})$
Initial interceptor heading γ_M	$150°$
Interceptor dynamics	First-Order
Dynamics time constant τ	$3 \cdot 10^{-5}\,\text{s}$

This scenario is simulated using the same initial conditions as Scenario 1(b) and will be compared to it.

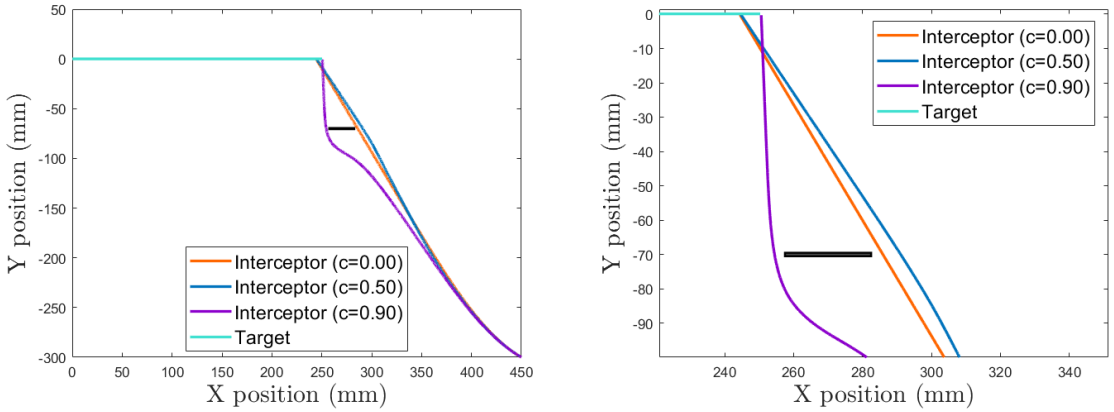

Figure 18: Interceptor trajectories with combined (flies) guidance law with dynamics (left: full view, right: zoomed).

In Scenario 1(b), we observed that the evasion occurred from the left side for all values of the gain. This time, as shown in Figure (18), only for the largest gain does the evasion remain

on the left, which is reasonable since the evasion started with larger acceleration component and the delay caused by the dynamics did not have enough time to affect the side of the evasion. For lower gains, the evasion is not significant, so the interceptor does not react strongly to the obstacle. When there is a delay, it takes time for the interceptor to "realize" the presence of the obstacle, and it therefore begins along the shortest path to the target, evading from the opposite side.

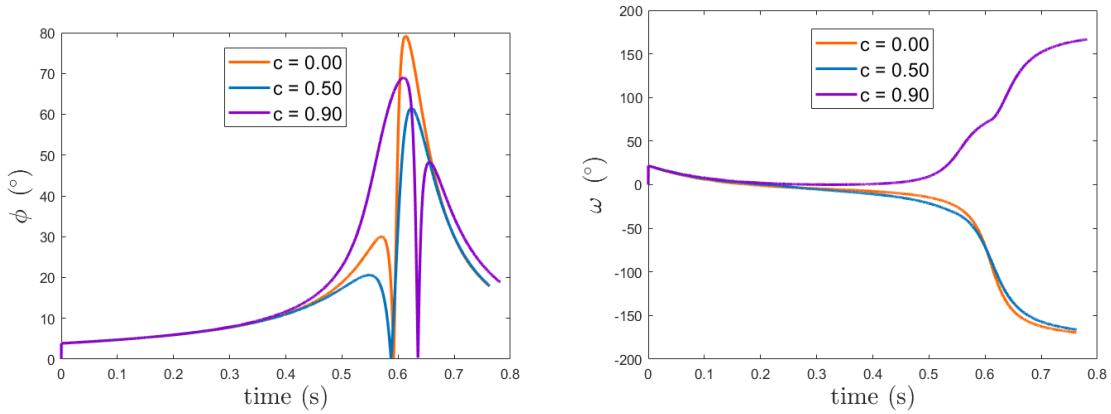

Figure 19: Left: Angular obstacle size ϕ over time. Right: The angle ω between v_M and r_{Mo} as function of time

In Figure (19), it can be seen that for evasion from the left with $c = 0.9$, ω is positive, while for evasion from the right, ω is negative, as expected. In the graph of the angular distance to the obstacle, a minimum is reached in all cases when the interceptor passes at the same y position as the obstacle.

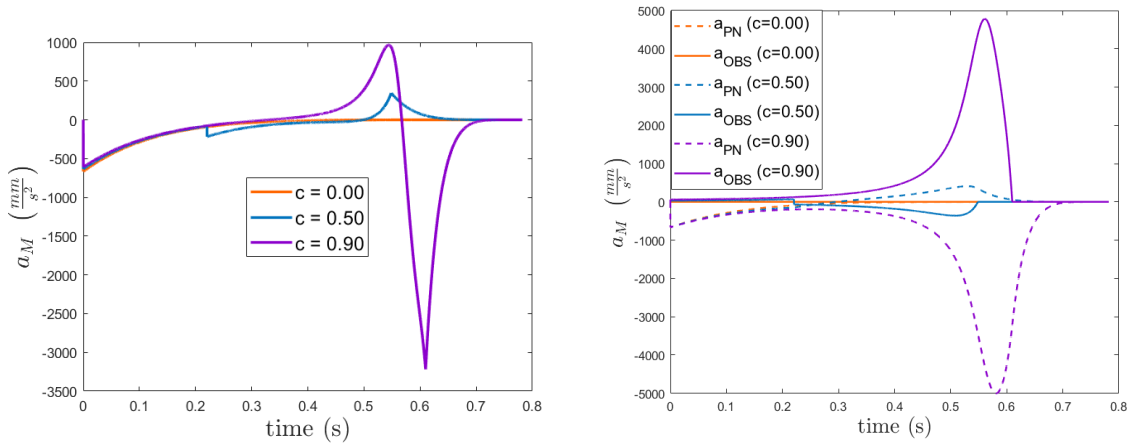

Figure 20: Left: Interceptor acceleration a_M over time. Right: Comparison between a_{PN} and a_{OBS} components.

In Figure (20) the change is particularly noticeable for $c = 0.5$, where this time the evasion component is very small. Due to the delay, the interceptor almost performs PN alone without significant evasion, so its graph resembles that of $c = 0$ more than that of $c = 0.9$.

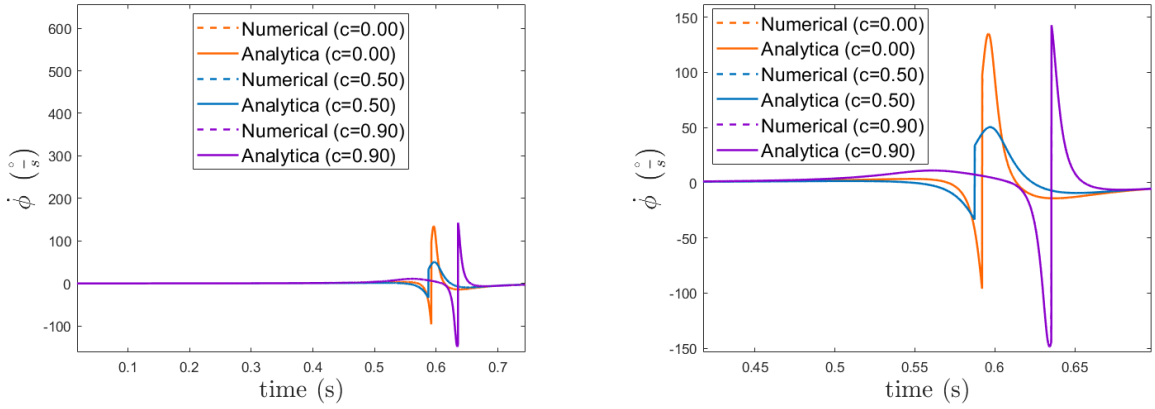

Figure 21: Rate of change of the obstacle's angular size $\dot{\phi}$ (left: full view, right: zoomed).

In Figure (21), we can observe the difference in the evasion trajectories corresponding to different gains. For $c = 0$ and $c = 0.5$, when the interceptor evades from the right, it passes at the height of the obstacle (reaching it with a negative $\dot{\phi}$) earlier, which is reasonable since it follows the shortest path to the target. In contrast, for $c = 0.9$, the interceptor takes a longer path, passing on the opposite side, so the peak in the derivative occurs later.

3.2 Comparison with a different avoidance guidance law

In this part, we will show a comparison between the combined guidance law used by flies to an optimal guidance law obtained by Kumar *et al.* in [43]. The proposed guidance law is an intercept angle guidance algorithm that minimizes control effort while ensuring a specified impact angle and point obstacle avoidance using bias-augmented proportional navigation. The guidance law obtained, which will be referred to as *'Kumar law'*, is as follows:

$$a_{MN} = 6V_c\dot{\lambda} + (3 + \frac{v'_M}{v'_T})a_{TN} + (\frac{2v'_M}{t_{go}})(\gamma_M + \gamma_T - \gamma_D) - a_{MNo} \tag{20}$$

while γ_D is represents the desired interception angle. In addition, a_{MN} , a_{TN} are the accelerations of the interceptor and target perpendicular to the initial target–interceptor LOS accordingly, and are defined:

$$a_{MN} = a_M cos(\gamma_M - \lambda_o) \tag{21}$$

$$a_{TN} = a_T cos(\gamma_T + \lambda_o) \tag{22}$$

and v'_M, v'_T are defined:

$$v'_T = v_T cos(\gamma_{To} + \lambda_0) \tag{23}$$

$$v'_M = v_M cos(\gamma_{Mo} - \lambda_0) \tag{24}$$

The signs denoted with X_o represent the initial value of X. Initial values are crucial in the guidance law described by Kumar *et al.* because the law is derived within a linearized engagement framework that assumes small deviations from the collision course at the outset. This means the initial line-of-sight (LOS) angle, initial missile and target positions, and initial velocities serve as baseline references for the guidance computation. The time to go is defined:

$$t_{go} = \frac{r}{V_c} \tag{25}$$

The term a_{MNo} is defined in the case of a single obstacle:

$$a_{MNo} = \frac{-3t_{go}}{tgo^2\Delta_1}\Psi_{R_1}(Z_{1c}) \tag{26}$$

while R_1 is the desired minimum distance from the obstacle and Δ_1 is defined:

$$\Delta_1 = t_f - t_{f_1} = t_{go} - t_{go_1} \tag{27}$$

and

$$t_{go_1} = \frac{r_{1o}}{V_m} \tag{28}$$

r_{1o} detonates the distance between the interceptor and the obstacle. The law is found for a point obstacle, and therefore, originally r_{1o} represents the distance to a fixed point. In this research, we investigate a case in which the obstacle is bar-shaped, so we use r_{1o} as the minimal distance between the bar and the interceptor in each moment.
The function $\psi_R(p)$ is defined:

$$\psi_R(p) = \begin{cases} 0 & \text{if } |p| \geq R \\ p - R & \text{if } 0 \leq p \leq R \\ p + R & \text{if } -R < p < 0 \end{cases} \tag{29}$$

And Z_{1c} is defined:

$$Z_{1c} = t_{\text{go}_1}^2 \left[v_M \dot{\theta}_0 + \left(1 + \frac{2\Delta_1}{t_{\text{go}}}\right) v_r \dot{\theta} - a_{TN} \left\{ \frac{1}{2} + \frac{\Delta_1}{t_{\text{go}}} \left(1 + \frac{v'_M}{v'_T}\right) \right\} \right] - \frac{v'_M \Delta_1}{t_{\text{go}}^2} (\gamma_M + \gamma_T - \gamma_D) \tag{30}$$

3.2.1 Scenario 4

The trajectories of the interceptor towards the interceptor while avoiding a single obstacle is shown in Figure (22) for both guidance laws. The parameters are described in Table 7. During all comparison scenarios we will use interception angle $\gamma_D = 20°$.

Table 7: Scenario 4 configuration summary

Parameter	**Value**
Interceptor initial position (x_{M0}, y_{M0})	$(240\,\text{mm}, 0\,\text{mm})$
Initial interceptor heading γ_M	$90°$
Initial target position (x_{T0}, y_{T0})	$(0.1\,\text{mm}, 300\,\text{mm})$
Obstacle center $(obs_{x_{\text{mid}}}, obs_{y_{\text{mid}}})$	$(215, 225)$ mm
Interceptor dynamics	None

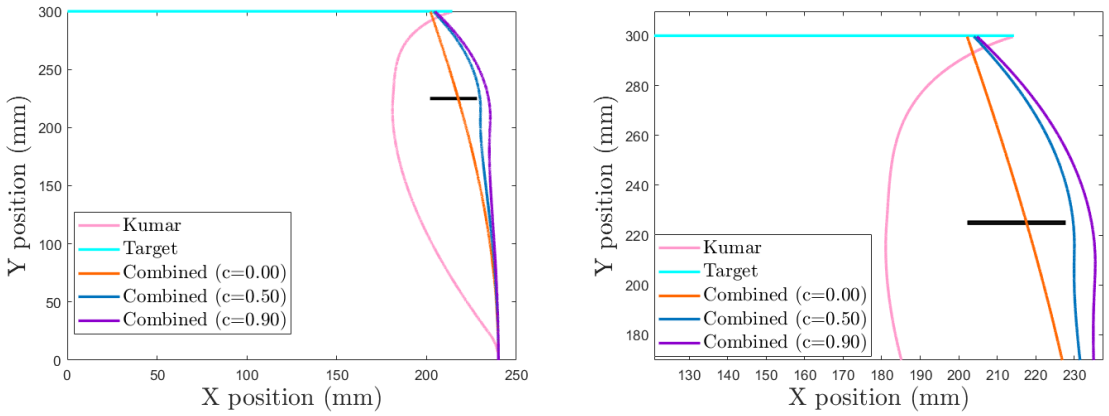

Figure 22: Trajectories for both guidance laws (left: full view, right: zoomed).

Next, we will compare the acceleration command for both laws in Figure (23).

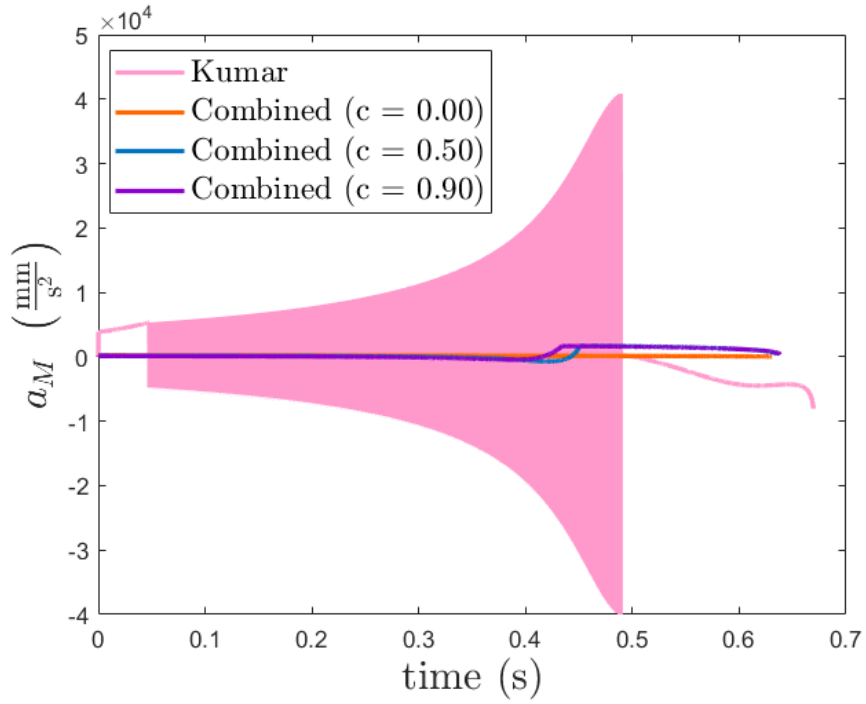

Figure 23: Acceleration command a_{Mc} for both guidance laws

The oscillation observed in the acceleration of the optimal (Kumar) guidance law may be attributed to the breakdown of linearization assumptions, which cannot handle sharp maneuvers or abrupt changes in path geometry. The law does not incorporate any control smoothing or damping, so when the missile's calculated avoidance acceleration switches rapidly—such as when it passes near the obstacle edge—large and sudden control signals result. Additionally, divisions by small values or logic discontinuities in the avoidance computation amplify these swings, especially in a simulated environment without actuator limits or filters.

3.2.2 Scenario 5

In this section, we will change the initial conditions and compare both guidance laws again for larger values of the gain c of 1 and 5. The parameters are described in Table 8.

Table 8: Scenario 5 configuration summary

Parameter	**Value**
Interceptor initial position (x_{M0}, y_{M0})	$(260\,\text{mm}, 0\,\text{mm})$
Initial interceptor heading γ_M	$110°$
Initial target position (x_{T0}, y_{T0})	$(0.1\,\text{mm}, 300\,\text{mm})$
Obstacle center $(obs_{x_{\text{mid}}}, obs_{y_{\text{mid}}})$	$(215, 225)$ mm
Interceptor dynamics	None

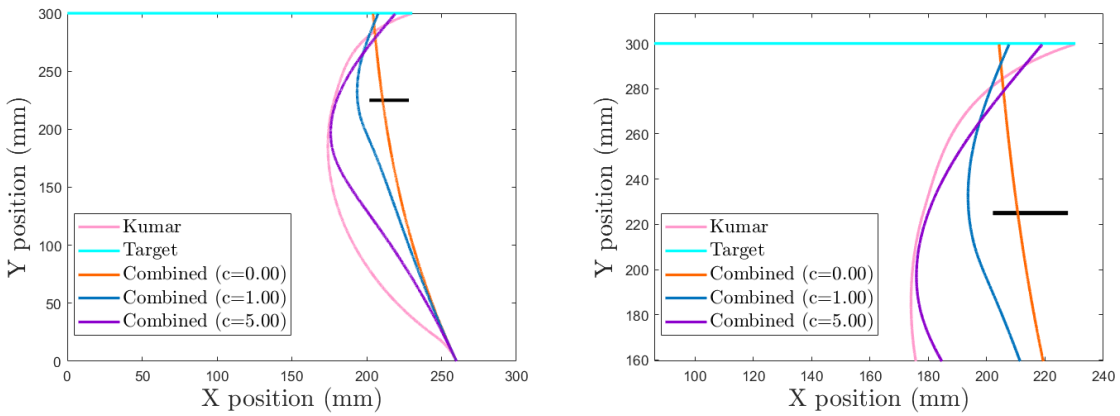

Figure 24: Interceptor and Target Trajectories for both guidance laws- different values of c- scenario 3.

In Figure (24), it can be observed that as the gain c increases, the evasion distance becomes larger, approaching that of Kumar law. For $c = 5$, a similarity can be seen between the evasion under the combined law and the evasion under Kumar law.

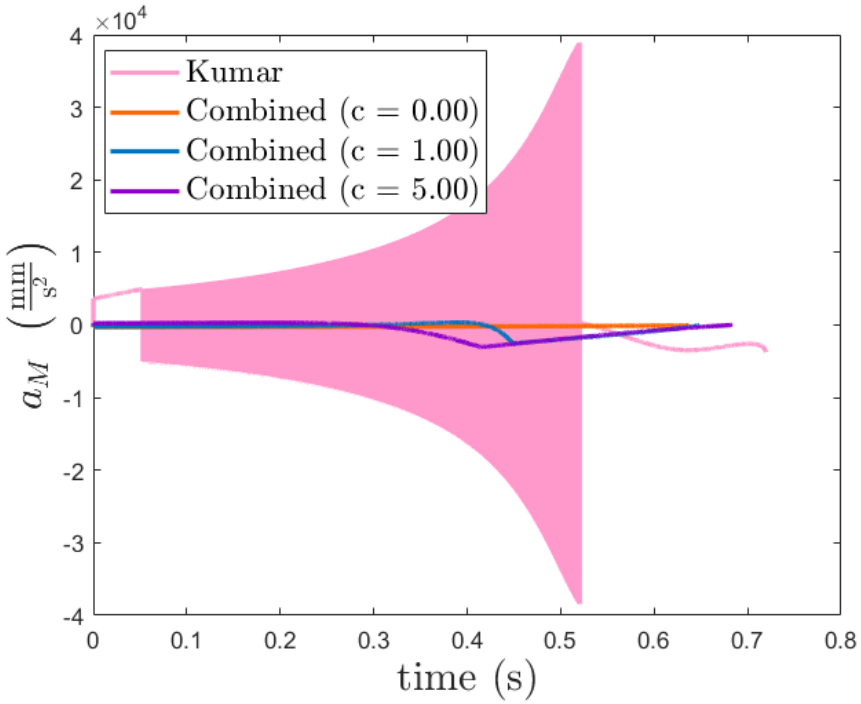

Figure 25: Interceptor Lateral Acceleration for both guidance laws- different values of c

It can be seen in Figure (25) that for this specific case of evasion from a single-bar obstacle under the combined law, where the evasion distance is almost identical to that of Kumar law, the required acceleration is much smaller.

3.2.3 Conclusions from the comparison

In this part of the research, a comparison is made between the obstacle avoidance guidance law inspired by flies and the optimal guidance law proposed in [43]. It is observed that for the fly-inspired law, low values of the gain parameter c bring to a smaller avoiding distance from the obstacle. Increasing the gain improves obstacle avoidance capability. In contrast,

the guidance law developed by Kumar *et al.* performs reliably with a large avoiding distance across various initial conditions without requiring gain adjustments, while maintaining stable trajectories. Moreover, the combined law is derived for the motion of a fly toward a target while evading a single obstacle, and its implementation is therefore limited to a single-bar obstacle. As a result, it is restricted in more general scenarios, unlike the optimal law, which can be applied even when multiple point obstacles are present. Overall, the optimal guidance law exhibits better performance (aside from the chattering) but requires more information in order to be used, which may be one reason why flies do not employ it.

4 Conclusions

This research investigates the combined guidance law for interception while avoiding an obstacle, which is found by Fabian *et al.* in [46]. The law is inspired by a miniature robber fly, and combines PN with an obstacle avoidance component. The avoidance behavior is proportional to the rate of change of the angular size of the obstacle. Differently from [46], in this research we focus on trajectories in which for PN - the interceptor is passing through the obstacle.

The implementation and simulation of this law revealed a clear dependence on the gain parameter c: when c is too low, the PN term dominates and the interceptor fails to avoid the obstacle; for sufficiently high values, the avoidance behavior becomes effective, resulting in significant clearance. However, the structure of the law—being a linear combination of two competing objectives—presents a challenge: the optimal value of c is not fixed and must be tuned carefully for each scenario, particularly under varying initial conditions.

When first-order dynamics were introduced to better represent physical limitations, the simulations showed delayed responses and smaller avoidance distances, with the interceptor sometimes steering around the obstacle from different sides. Additionally, while a FOV constraint was tested, it had minimal effect in this context, likely due to the large FOV that was chosen, the short engagement time and the small spatial scale of the scenario.

To benchmark the combined law, we compared it against an optimal avoidance strategy designed for a point obstacle, found by Kumar *et al.* in [43]. The optimal law yielded consistent interception and obstacle clearance but at the cost of high-frequency acceleration oscillations—likely due to the mismatch between the rectangular shape of the obstacle and the point-based assumptions in the optimal model. For comparison, we evaluated the Kumar avoidance law, which employs a geometric construction based on the angle between the line-of-sight and the tangential contact point on the obstacle boundary. Although Kumar's law effectively produces avoidance maneuvers, it suffers from divergence in the commanded acceleration. In contrast, the combined law maintains bounded accelerations and offers controllable trade-offs between interception aggressiveness and avoidance strength, though it requires careful parameter tuning.

These findings support and extend insights from the literature. Many animals, as reviewed, employ simple guidance laws—such as Proportional Navigation—and some exhibit hybrid or mixed guidance laws, adjusting in real time to obstacles, as seen in flies in [46]. The simulations here affirm that such biologically inspired laws can achieve effective obstacle avoidance, but also highlight the trade-offs between simplicity, robustness, and dynamic responsiveness. While nature-inspired models offer valuable frameworks, their practical application in engineered systems requires careful parameter tuning and consideration of dynamic effects.

5 Possible Future Work

Future work could focus on determining the optimal value of the gain parameter c in the combined guidance law presented in [46], particularly under varying initial conditions, to enhance performance and robustness. In addition, implementing the combined guidance law on robotic

platforms would allow for experimental validation and exploration of real-world applications. Further research might also examine the geometric rule of the avoidance maneuver performed when intercepting a target while avoiding bar-shaped obstacles. Extending the law—originally designed for point-like obstacles—to accommodate extended or non-point obstacles, as was done with Kumar's guidance law, represents another relevant avenue. Another interesting direction can be to implement the combined law on an obstacle with a different shape than a bar.

In addition, finding other options to implement the limited field of view of the interceptor is a possible direction. Finally, comparing the trajectories generated by the flies guidance law with optimal paths computed using optimization tools such as FALCON could provide insight into the law's efficiency and how closely it approximates optimal behavior.

References

[1] Neryahu A Shneydor. *Missile guidance and pursuit: kinematics, dynamics and control*. Elsevier, 1998.

[2] Alfred M Bruckstein. Why the ant trails look so straight and nice. *The Mathematical Intelligencer*, 15(2):59–62, 1993.

[3] Suzanne Amador Kane, Andrew H Fulton, and Lee J Rosenthal. When hawks attack: animal-borne video studies of goshawk pursuit and prey-evasion strategies. *Journal of Experimental Biology*, 218(2):212–222, 2015.

[4] Michael F Land and TS Collett. Chasing behaviour of houseflies (fannia canicularis) a description and analysis. *Journal of comparative physiology*, 89:331–357, 1974.

[5] Betty S Lanchester and RF Mark. Pursuit and prediction in the tracking of moving food by a teleost fish (acanthaluteres spilomelanurus). *Journal of Experimental Biology*, 63(3):627–645, 1976.

[6] Matthew J McHenry, Jacob L Johansen, Alberto P Soto, Brian A Free, Derek A Paley, and James C Liao. The pursuit strategy of predatory bluefish (pomatomus saltatrix). *Proceedings of the Royal Society B*, 286(1897):20182934, 2019.

[7] Kaushik Ghose, Timothy K Horiuchi, PS Krishnaprasad, and Cynthia F Moss. Echolocating bats use a nearly time-optimal strategy to intercept prey. *PLoS biology*, 4(5):e108, 2006.

[8] Suzanne Amador Kane and Marjon Zamani. Falcons pursue prey using visual motion cues: new perspectives from animal-borne cameras. *Journal of Experimental Biology*, 217(2):225–234, 2014.

[9] Brett R Fajen and William H Warren. Visual guidance of intercepting a moving target on foot. *Perception*, 33(6):689–715, 2004.

[10] Michael K McBeath, Dennis M Shaffer, and Mary K Kaiser. How baseball outfielders determine where to run to catch fly balls. *Science*, 268(5210):569–573, 1995.

[11] Dennis M Shaffer, Scott M Krauchunas, Marianna Eddy, and Michael K McBeath. How dogs navigate to catch frisbees. *Psychological science*, 15(7):437–441, 2004.

[12] Ziv Kassner and Gal Ribak. Role of side-slip flight in target pursuit: blue-tailed damselflies (ischnura elegans) avoid body rotation while approaching a moving perch. *Journal of Comparative Physiology A*, 204:561–577, 2018.

[13] Paul Zarchan. *Tactical and strategic missile guidance*. American Institute of Aeronautics and Astronautics, Inc., 2012.

[14] Caroline H Brighton, Adrian LR Thomas, and Graham K Taylor. Terminal attack trajectories of peregrine falcons are described by the proportional navigation guidance law of missiles. *Proceedings of the National Academy of Sciences*, 114(51):13495–13500, 2017.

[15] Caroline H Brighton, Katherine E Chapman, Nicholas C Fox, and Graham K Taylor. Attack behaviour in naive gyrfalcons is modelled by the same guidance law as in peregrine falcons, but at a lower guidance gain. *Journal of Experimental Biology*, 224(5):jeb238493, 2021.

[16] Natalia Pérez-Campanero Antolín and Graham K Taylor. Gap selection and steering during obstacle avoidance in pigeons. *Journal of Experimental Biology*, 226(2):jeb244215, 2023.

[17] Samuel T Fabian, Mary E Sumner, Trevor J Wardill, Sergio Rossoni, and Paloma T Gonzalez-Bellido. Interception by two predatory fly species is explained by a proportional navigation feedback controller. *Journal of The Royal Society Interface*, 15(147):20180466, 2018.

[18] Andreas F Haselsteiner, Cole Gilbert, and Z Jane Wang. Tiger beetles pursue prey using a proportional control law with a delay of one half-stride. *Journal of the Royal Society Interface*, 11(95):20140216, 2014.

[19] Caroline H Brighton and Graham K Taylor. Hawks steer attacks using a guidance system tuned for close pursuit of erratically manoeuvring targets. *Nature communications*, 10(1):2462, 2019.

[20] James A Kempton, Caroline H Brighton, Lydia A France, Marco KleinHeerenbrink, Sofia Miñano, James Shelton, and Graham K Taylor. Visual versus visual-inertial guidance in hawks pursuing terrestrial targets. *Journal of the Royal Society Interface*, 20(203):20230071, 2023.

[21] Leandre Varennes, Holger G Krapp, and Stephane Viollet. Two pursuit strategies for a single sensorimotor control task in blowfly. *Scientific reports*, 10(1):20762, 2020.

[22] Matteo Mischiati, Huai-Ti Lin, Paul Herold, Elliot Imler, Robert Olberg, and Anthony Leonardo. Internal models direct dragonfly interception steering. *Nature*, 517(7534):333–338, 2015.

[23] Akiko Mizutani, Javaan S Chahl, and Mandyam V Srinivasan. Motion camouflage in dragonflies. *Nature*, 423(6940):604–604, 2003.

[24] Eric W Justh and PS Krishnaprasad. Steering laws for motion camouflage. *Proceedings of the Royal Society A: Mathematical, Physical and Engineering Sciences*, 462(2076):3629–3643, 2006.

[25] Trevor J Wardill, Samuel T Fabian, Ann C Pettigrew, Doekele G Stavenga, Karin Nordström, and Paloma T Gonzalez-Bellido. A novel interception strategy in a miniature robber fly with extreme visual acuity. *Current Biology*, 27(6):854–859, 2017.

[26] Dirk Reichardt and Jeong Shick. Collision avoidance in dynamic environments applied to autonomous vehicle guidance on the motorway. In *Proceedings of the Intelligent Vehicles' 94 Symposium*, pages 74–78. IEEE, 1994.

[27] Wael Ben-Messaoud, Michel Basset, Jean-Philippe Lauffenburger, and Rodolfo Orjuela. Smooth obstacle avoidance path planning for autonomous vehicles. In *2018 IEEE International Conference on Vehicular Electronics and Safety (ICVES)*, pages 1–6. IEEE, 2018.

[28] Evan Lowe and Levent Guvenc. Autonomous vehicle emergency obstacle avoidance maneuver framework at highway speeds. *Electronics*, 12(23):4765, 2023.

[29] Animesh Chakravarthy and Debasish Ghose. Obstacle avoidance in a dynamic environment: A collision cone approach. *IEEE Transactions on Systems, Man, and Cybernetics-Part A: Systems and Humans*, 28(5):562–574, 1998.

[30] Paolo Fiorini and Zvi Shiller. Motion planning in dynamic environments using velocity obstacles. *The international journal of robotics research*, 17(7):760–772, 1998.

[31] Lima Agnel Tony, Debasish Ghose, and Animesh Chakravarthy. Avoidance maps: A new concept in uav collision avoidance. In *2017 International Conference on Unmanned Aircraft Systems (ICUAS)*, pages 1483–1492. IEEE, 2017.

[32] Lima A Tony, Debasish Ghose, and Animesh Chakravarthy. Precision uav collision avoidance using computationally efficient avoidance maps. In *2018 AIAA Guidance, Navigation, and Control Conference*, page 0875, 2018.

[33] C Giovannangeli, M Heymann, E Rivlin, and V Kordic. Pursuit-evasion games in presence of obstacles in unknown environments: towards an optimal pursuit strategy. *Cutting edge robotics*, 2010:47–80, 2010.

[34] Igor Škrjanc and Gregor Klančar. Optimal cooperative collision avoidance between multiple robots based on bernstein–bézier curves. *Robotics and Autonomous systems*, 58(1):1–9, 2010.

[35] KG Jolly, R Sreerama Kumar, and R Vijayakumar. A bezier curve based path planning in a multi-agent robot soccer system without violating the acceleration limits. *Robotics and Autonomous Systems*, 57(1):23–33, 2009.

[36] Saurabh Upadhyay and Ashwini Ratnoo. Continuous-curvature path planning with obstacle avoidance using four parameter logistic curves. *IEEE Robotics and Automation Letters*, 1(2):609–616, 2016.

[37] Tomas Berglund, Andrej Brodnik, Håkan Jonsson, Mats Staffanson, and Inge Soderkvist. Planning smooth and obstacle-avoiding b-spline paths for autonomous mining vehicles. *IEEE transactions on automation science and engineering*, 7(1):167–172, 2009.

[38] Kyle Klein and Subhash Suri. Catch me if you can: Pursuit and capture in polygonal environments with obstacles. In *Proceedings of the AAAI Conference on Artificial Intelligence*, volume 26, pages 2010–2016, 2012.

[39] Su-Cheol Han, Hyochoong Bang, and Chang-Sun Yoo. Proportional navigation-based collision avoidance for uavs. *International Journal of Control, Automation and Systems*, 7:553–565, 2009.

[40] Paul M Zapotezny-Anderson and Jason J Ford. Optimal-stopping control for airborne collision avoidance and return-to-course flight. In *2011 Australian Control Conference*, pages 155–160. IEEE, 2011.

[41] Martin Weiss and Tal Shima. Linear quadratic optimal control-based missile guidance law with obstacle avoidance. *IEEE Transactions on Aerospace and Electronic Systems*, 55(1):205–214, 2018.

[42] Martin Weiss and Tal Shima. Minimum effort pursuit/evasion guidance with specified miss distance. *Journal of Guidance, Control, and Dynamics*, 39(5):1069–1079, 2016.

[43] Shashi Ranjan Kumar, Martin Weiss, and Tal Shima. Minimum-effort intercept angle guidance with multiple-obstacle avoidance. *Journal of Guidance, Control, and Dynamics*, 41(6):1355–1369, 2018.

[44] Bhargav Jha, Ronny Tsalik, Martin Weiss, and Tal Shima. Cooperative guidance and collision avoidance for multiple pursuers. *Journal of Guidance, Control, and Dynamics*, 42(7):1506–1518, 2019.

[45] Soulaimane Berkane, Andrea Bisoffi, and Dimos V Dimarogonas. A hybrid controller for obstacle avoidance in an n-dimensional euclidean space. In *2019 18th European Control Conference (ECC)*, pages 764–769. IEEE, 2019.

[46] Samuel T Fabian, Mary E Sumner, Trevor J Wardill, and Paloma T Gonzalez-Bellido. Avoiding obstacles while intercepting a moving target: a miniature fly's solution. *Journal of Experimental Biology*, 225(4):jeb243568, 2022.

[47] Caroline H Brighton, James A Kempton, Lydia A France, Marco KleinHeerenbrink, Sofía Miñano, and Graham K Taylor. Obstacle avoidance in aerial pursuit. *Current Biology*, 33(15):3192–3202, 2023.

[48] Annemarie Surlykke, Kaushik Ghose, and Cynthia F Moss. Acoustic scanning of natural scenes by echolocation in the big brown bat, eptesicus fuscus. *Journal of Experimental Biology*, 212(7):1011–1020, 2009.

[49] RM Robertson and AG Johnson. Retinal image size triggers obstacle avoidance in flying locusts. *Naturwissenschaften*, 80:176–178, 1993.

[50] Brett R Fajen, William H Warren, Selim Temizer, and Leslie Pack Kaelbling. A dynamical model of visually-guided steering, obstacle avoidance, and route selection. *International Journal of Computer Vision*, 54:13–34, 2003.

6 Appendix A- finding ϕ and its derivative

In this section, the definition of the angles will be shown, as well as their derivative in time. The obstacle is a static rectangular bar, as described in Figure (26), in which:

- (x_L, y_L) represents the x, y-position of the lower left vertex of the rectangle
- (x_R, y_R) represents the x, y-position of the lower right vertex of the rectangle
- (x_{mid}, y_{mid}) is the midpoint of the lower (horizontal) side of the rectangle
- (x_M, y_M) represents the location of the interceptor

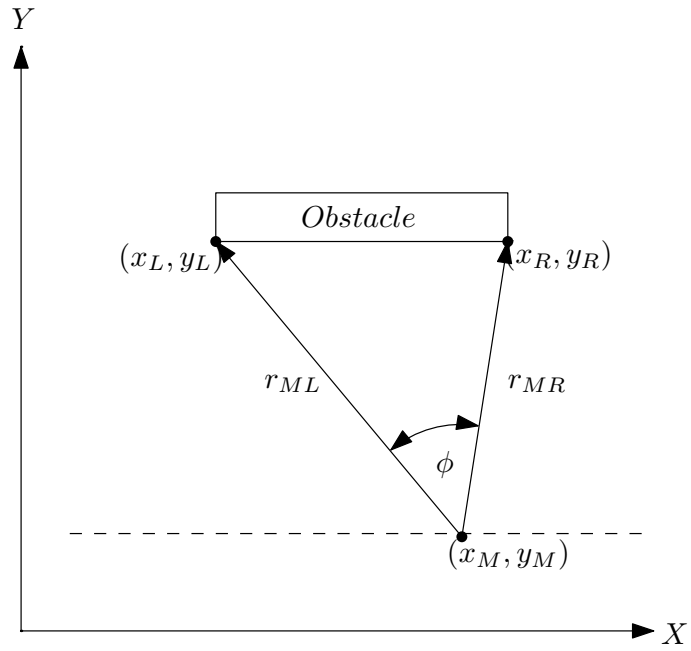

Figure 26: Obstacle description

Finding ϕ

We will describe the angle ϕ with the dot product between $\vec{r}_{MR}$ and $\vec{r}_{ML}$, while

$$\vec{r}_{MR} = (x_R - x_M, y_R - y_M, 0) \tag{31}$$

$$\vec{r}_{ML} = (x_L - x_M, y_L - y_M, 0) \tag{32}$$

Since the obstacle is horizontal, $y_R = y_L$. so we will denote both by y_o. We will also denote:

$$dx_R = x_R - x_M \tag{33}$$

$$dx_L = x_L - x_M \tag{34}$$

$$dy = y_0 - y_M \tag{35}$$

$$r_{MR} = \sqrt{(x_R - x_M)^2 + (y_o - y_M)^2} = \sqrt{dx_R^2 + dy_2} \tag{36}$$

$$r_{ML} = \sqrt{(x_L - x_M)^2 + (y_L - y_M)^2} = \sqrt{dx_L^2 + dy^2} \tag{37}$$

$$\cos(\phi) = \frac{\vec{r}_{MR} \cdot \vec{r}_{ML}}{r_{MR} r_{ML}} \tag{38}$$

$$\sin(\phi) = \frac{|\vec{r}_{MR} \times \vec{r}_{ML}|}{r_{MR}\, r_{ML}} \tag{39}$$

And of course:

$$tan(\phi) = \frac{sin(\phi)}{cos(\phi)} \tag{40}$$

And therefore:

$$tan(\phi) = \frac{|\vec{r}_{MR} \times \vec{r}_{ML}|}{\vec{r}_{MR} \cdot \vec{r}_{ML}} \tag{41}$$

$$\phi = \arctan\left(\frac{|\vec{r}_{MR} \times \vec{r}_{ML}|}{\vec{r}_{MR} \cdot \vec{r}_{ML}}\right) \tag{42}$$

$$|\vec{r}_{MR} \times \vec{r}_{ML}| = dy(dx_R - dx_L) \tag{43}$$

$$\vec{r}_{MR} \cdot \vec{r}_{ML} = dx_R dx_L + dy^2 \tag{44}$$

Finally,

$$\phi = \left|\arctan\left(\frac{dy \cdot (dx_R - dx_L)}{dx_R \cdot dx_L + dy^2}\right)\right| \tag{45}$$

In practice, we are interested in the magnitude of the angle, which is always a non-negative quantity. Therefore, we take the absolute value of the arctangent expression to ensure that $\phi \geq 0$.

$$\phi = \begin{cases} \arctan\left(\frac{dy \cdot (dx_R - dx_L)}{dx_R \cdot dx_L + dy^2}\right), & \text{if } \phi \geq 0 \\ -\arctan\left(\frac{dy \cdot (dx_R - dx_L)}{dx_R \cdot dx_L + dy^2}\right), & \text{if } \phi < 0 \end{cases} \tag{46}$$

Finding the derivative of ϕ

To find the derivative in time of the angle ϕ we will use that:

$$\dot{dx_R} = \dot{dx_L} = -v_{Mx} \tag{47}$$

$$\dot{dy} = -v_{My} \tag{48}$$

We begin with the expression for the angle ϕ:

$$\phi = \arctan\left(\frac{dy \cdot (dx_R - dx_L)}{dx_R \cdot dx_L + dy^2}\right)$$

Let:

$$f = \frac{dy \cdot (dx_R - dx_L)}{dx_R \cdot dx_L + dy^2} \quad \Rightarrow \quad \phi = \arctan(f) \tag{49}$$

Then, by the chain rule:

$$\dot{\phi} = \frac{1}{1 + f^2} \cdot \dot{f} \tag{50}$$

Define the numerator and denominator of f:

$$N = dy \cdot (dx_R - dx_L), \quad D = dx_R \cdot dx_L + dy^2 \quad \Rightarrow \quad f = \frac{N}{D} \tag{51}$$

Then:

$$\dot{f} = \frac{\dot{N} \cdot D - N \cdot \dot{D}}{D^2} \tag{52}$$

We compute $\dot{N}$ and $\dot{D}$:

1. Compute $\dot{N}$:

$$\dot{N} = \frac{d}{dt}\left[dy \cdot (dx_R - dx_L)\right] = \dot{dy} \cdot (dx_R - dx_L) + dy \cdot (\dot{dx}_R - \dot{dx}_L) \tag{53}$$

Given:

$$\dot{dx}_R = \dot{dx}_L = -v_{Mx}, \quad \dot{dy} = -v_{My} \tag{54}$$

So:

$$\dot{dx}_R - \dot{dx}_L = -v_{Mx} - (-v_{Mx}) = 0 \quad \Rightarrow \quad \dot{N} = -v_{My} \cdot (dx_R - dx_L) \tag{55}$$

2. Compute $\dot{D}$:

$$\dot{D} = \frac{d}{dt}(dx_R \cdot dx_L + dy^2) = \dot{dx}_R \cdot dx_L + dx_R \cdot \dot{dx}_L + 2 \cdot dy \cdot \dot{dy} \tag{56}$$

Substituting:

$$\dot{D} = (-v_{Mx}) \cdot dx_L + dx_R \cdot (-v_{Mx}) + 2 \cdot dy \cdot (-v_{My}) = -v_{Mx}(dx_L + dx_R) - 2dyv_{My} \tag{57}$$

3. Plug into $\dot{f}$:

$$\dot{f} = \frac{[-v_{My}(dx_R - dx_L)] \cdot (dx_R dx_L + dy^2) - [dy(dx_R - dx_L)] \cdot [-v_{Mx}(dx_L + dx_R) + (-2dyv_{My})]}{(dx_R dx_L + dy^2)^2} \tag{58}$$

4. Finally, plug into $\dot{\phi}$:

$$\dot{\phi} = \begin{cases} \frac{1}{1+f^2} \cdot \dot{f}, & \text{if } \phi \geq 0 \\ -\frac{1}{1+f^2} \cdot \dot{f}, & \text{if } \phi < 0 \end{cases} \tag{59}$$

This accounts for the time derivative of the absolute angle $\phi = |\arctan(f)|$, and this is the complete expression for the time derivative of the angle ϕ.